Central-Tapped Node Linked Modular Fault-Tolerance Topology for SRM Applications

Yihua Hu, *Member, IEEE*, Chun Gan, *Student Member, IEEE*, Wenping Cao, *Senior Member, IEEE*,
Wuhua Li, *Member, IEEE*, and Stephen J. Finney

***Abstract*—Electric vehicles (EVs) and hybrid electric vehicles (HEVs) can reduce greenhouse gas emissions while switched reluctance motor (SRM) is one of the promising motor for such applications. This paper presents a novel SRM fault-diagnosis and fault-tolerance operation solution. Based on the traditional asymmetric half-bridge topology for the SRM driving, the central tapped winding of the SRM in modular half-bridge configuration are introduced to provide fault-diagnosis and fault-tolerance functions, which are set idle in normal conditions. The fault diagnosis can be achieved by detecting the characteristic of the excitation and demagnetization currents. An SRM fault-tolerance operation strategy is also realized by the proposed topology, which compensates for the missing phase torque under the open-circuit fault, and reduces the unbalanced phase current under the short-circuit fault due to the uncontrolled faulty phase. Furthermore, the current sensor placement strategy is also discussed to give two placement methods for low cost or modular structure. Simulation results in MATLAB/Simulink and experiments on a 750-W SRM validate the effectiveness of the proposed strategy, which may have significant implications and improve the reliability of EVs/HEVs.**

***Index Terms*—Central tapped node, electric vehicles, fault diagnosis, fault tolerance, switched reluctance motor (SRM), traction drives.**

NOMENCLATURE

D	PWM duty cycle.
i_a, i_b, i_c	Currents for phases *A*, *B*, and *C*.
$i'_{\max}$	Phase current peak when faulted.
$i_{\max}$	Phase current peak when normal.
Δi	Hysteresis window.
N_r	Rotor poles.
K_L	Inductance slope when normal.
K'_i	Current slope when normal.
K'_L	Inductance slope when faulted.
K_i	Current slope when faulted.
$L_{\min}$	Minimum of the phase inductance.
$L_{\max}$	Maximum of the phase inductance.
T^*	Given load torque.
T	Instantaneous torque.
T_{av}	Average electromagnetic torque of one phase when normal.
T'_{av}	Average electromagnetic torque of one phase when faulted.
U_{in}	Bus voltage.
ω_r	Angular velocity.
θ_{on}	Turn-on angle.
θ_{off}	Turn-off angle.

I. INTRODUCTION

CURRENTLY, electric vehicles (EVs) and hybrid electric vehicles (HEVs) provide a low-pollution and high-efficiency solution to the depletion of fossil fuels and environmental problems, and thus, are under wide development across the world [1], [2]. Switched reluctance motors (SRMs) are becoming a mature technology for EV/HEV applications and are also considered to have commercial potentials for massive global markets due to their nonreliance on rare earth materials and a wide torque–speed range, in addition to their robust mechanical structure, low cost and high efficiency [3]–[7]. For EV/HEV applications, high reliability and fault tolerance is critically important as they involve human lives.

The SRM drive system is mainly composed by two parts: power electronics and motors [8]. For EV/HEV applications, the switching devices are prone to failure, especially in harsh environments such as vehicular conditions [9]. Based on the widely used asymmetrical half-bridge drive topology, the power electronics faulty conditions such as short-circuits and open-circuits are studied in [10]–[16]. In [11], the bus current is employed to distinguish open-circuit faults and short-circuit faults in power electronics converters. In [12], two on-line fault-diagnosis methods based on analysis of bus current or freewheeling current are developed to distinguish short circuits and open circuits. In [13], the switching device fault diagnosis including open circuit and short circuit is achieved by analysis of phase current without additional hardware investment. The FFT algorithm is also introduced to analyze the power converter supply current of phase absence fault in [14]. A method to predict the SRM drive performance under normal and fault operating conditions is proposed in [15], which uses a genetic-algorithm-based artificial neural networks, showing a fast and accurate prediction. In

Manuscript received September 29, 2014; revised December 7, 2014 and January 28, 2015; accepted March 9, 2015. Date of publication March 18, 2015; date of current version September 29, 2015. This work was supported by the EPSRC of UK (EP/L00089X/1). Recommended for publication by Associate Editor J. A. Pomilio.

Y. Hu is with the College of Electrical Engineering, Zhejiang University, Hangzhou 310027, China, and is also with the Department of Electronic and Electrical Engineering, University of Strathclyde, Glasgow G1 1XQ, U.K. (e-mail: huyihuacumt@126.com).

C. Gan and W. Li are with the College of Electrical Engineering, Zhejiang University, Hangzhou 310027, China (e-mail: ganchun.cumt@163.com; woohualee@zju.edu.cn).

W. Cao is with the School of Electronics, Electrical Engineering and Computer Science, Queen's University Belfast, Belfast BT7 1NN, U.K. (e-mail: w.cao@qub.ac.uk).

S. J. Finney is with the Department of Electronic and Electrical Engineering, University of Strathclyde, Glasgow G1 1XQ, U.K. (e-mail: stephen.finney@strath.ac.uk).

Digital Object Identifier 10.1109/TPEL.2015.2414664

[16], a fuzzy inference system is employed to characterize the SRM drives under normal and fault operations. The other research field is motor fault diagnosis. The winding short-circuit and open-circuit are the common faults in electric machines [17]. Pole short and few turns shorted of phase winding are discussed in [18]. In [19], injecting high-frequency diagnostic pulses to the motor windings is proposed to locate faulty phase and categorize the fault type.

In order to improve the SRM fault-tolerance ability, hardware and software can be employed to achieve fault-tolerance operation. For fault-tolerance control, artificial neural network, genetic algorithms, and the time dynamic models are developed for normal and abnormal condition control of the SRM [20]. The Fuzzy controller without a model is proposed in [21] to improve the faulty performance of the SRM. For hardware improvement, a multiphase SRM is developed to improve fault tolerance [22], [23]. The axial-flux-configuration-based, five-phase SRM is developed for EV application [23]. In order to improve the reliability of the SRM driving system, a dual-channel SRM is developed and fault-tolerance strategy is also discussed in [24]. The modular stator SRM is proposed in [25], which is convenient for replacing the fault winding. In [26], a double-layer-per-phase isolated SRM is also investigated, which cannot only improve the fault-tolerant capability, but also achieve higher torque and low noise. Furthermore, segmental stator SRM with modular construction is proposed for fault-tolerance application [27]. In [28], two extra switching devices are added in the traditional asymmetric half-bridge topology for an 8/6 SRM drive system to decrease the impact of a fault. However, the proposed fault-tolerance topology is without module structure and only accustoms limited fault condition. A decentralized phase driving topology is developed in [29] to make full use of independence of phase windings; while a lot of half asymmetric modular. In the absence of position sensors, a fault-tolerance control strategy is proposed in [30] to deal with the absent phase operation. In [31], a fault-tolerance scheme is proposed for the SRM drive that is driven by a three-phase bridge inverter when the phase windings are connected in star. The fault characteristics of the SRM drive under short- and open-circuit fault operations are analyzed in details in [32], and a fault-tolerant control method is presented. However, the phase absence operation in open-circuit condition and setting the turn-off angle advanced in short-circuit condition still causes a large torque ripples.

Although hardware and software fault tolerance have been developed, the hardware changes the driving topology of the SRM or design the new structure of the SRM that limits the wide application. Furthermore, by software, the fault-diagnosis and fault-tolerance operation can be achieved without changing the traditional SRM drive topology; but the fault-diagnosis method is complex and fault toleration can be realized in limited fault condition. So, we need the fault-diagnosis and fault-tolerance strategy is equipped with the following characteristics:

1) no/little change to the traditional SRM drive topology;
2) easy fault-diagnosis and fault-tolerance operation at extreme fault conditions;
3) modular structure and convenient for industrial applications.

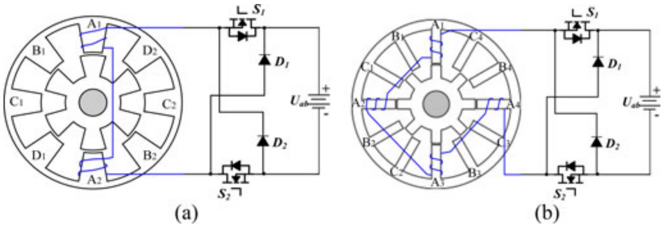

Fig. 1. Basic winding structure of SRM, (a) 8/6 SRM, (b) 12/8 SRM.

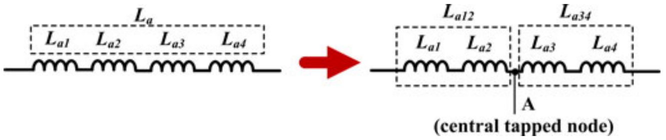

Fig. 2. Central-tapped winding of a 12/8 SRM.

In this paper, in order to satisfy the mentioned requirements, a new modular fault-tolerance topology is proposed on the basis of the traditional SRM driving topology; and the corresponding fault-diagnosis and fault-tolerance schemes are proposed by tradeoff hardware and software. This paper is organized as follows: Section II describes the proposed fault-tolerance topology, and fault-diagnosis method. Section III builds the mathematical model of the SRM under fault-tolerance condition and gives the fault-tolerance control strategy. Section IV discusses the current sensors placement. Section V presents experimental results and their analysis, followed by the conclusions in Section VI.

II. FAULT-DIAGNOSIS TOPOLOGY AND STRATEGY

New techniques are developed to improve the system performance under various faults, including switching device faults, phase winding, and short-circuit faults. The fault-tolerant strategy is to make changes to hardware as little as possible on the basis of the traditional SRM topology.

A. Proposed Fault-Tolerance Topology

Traditionally, the SRM phase windings are composed of an even number of series connected windings, as shown in Fig. 1. Thus, central-tapped windings are formed, which can be easily designed in 8/6 or 12/8 SRM. Fig. 2 shows the traditional 12/8 SRM winding connection, in which L_{a1}, L_{a2}, L_{a3}, and L_{a4} represent for four windings of one SRM phase; the central tapped node A of phase L_a is developed as shown in Fig. 2. One phase of the SRM drive circuit is composed by the traditional asymmetrical half-bridge topology and phase winding; the whole circuit can be divided into two parts: left part and right part, as shown in Fig. 3; each part has the same components, including diode, switching device and phase winding. The two parts have the characteristics of axial symmetry that can be employed in fault-tolerance operation. When the central tapped node is connected with positive node of power supply source, the left part of the converter is bypassed that can block the left part fault. The same method, when the central tapped node A is connected

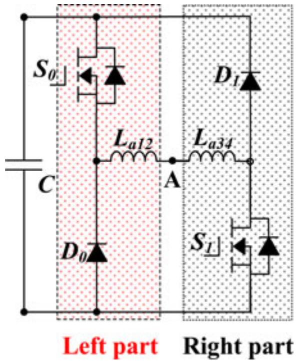

Fig. 3. Two parts of phase converter.

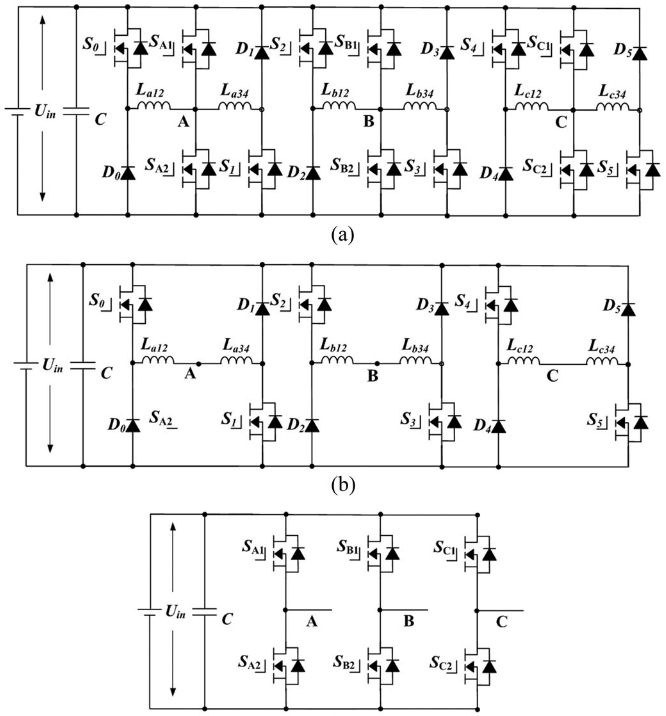

(a)

(b)

(c)

Fig. 4. Proposed topology for SRM fault-tolerance operation. (a) Proposed fault-tolerance topology. (b) Main topology for SRM. (c) Fault-tolerance module.

with negative node of power supply source, the right part of the converter is bypassed that can block the fault from right part.

On the basis of the central tapped node and axial symmetry characteristics of the traditional drive topology, the proposed fault-tolerance topology is presented in Fig. 4. Fig. 4(a) is the main driving topology composed by main topology (traditional asymmetrical half bridge) as Fig. 4(b), and fault-tolerance module as Fig. 4(c). The fault-tolerance module is the traditional three-phase half-bridge modular. The half-bridge central nodes are connected with central tapped node of phase windings, which are *A*, *B*, and *C*, respectively. Three-phase half bridge is employed to approach fault-tolerance operation. The proposed topology has the characteristics of modular structure; on the base of the traditional asymmetrical half-bridge topology, only one three-phase bridge modular is needed. The basic structure of the SRM is almost not changed. In normal conditions, the proposed topology works as traditional asymmetrical half-bridge topology; the fault-tolerance module is in idle condition that makes the proposed converter has the same efficiency as the traditional asymmetrical half-bridge topology. The fault-tolerance module works only at fault condition.

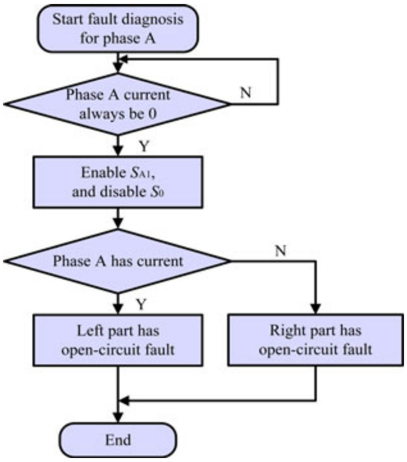

Fig. 5. Flowchart for the diagnosis of the open-circuit fault.

B. Switching Device Faults and Phase Winding Open-Circuit Faults

Switching device faults and phase winding open-circuit faults are common fault phenomena. In the traditional asymmetrical half-bridge converter, there are two switching devices for each phase; and each phase have four windings for a 12/8 SRM. When there is no current in the excitation region in phase L_a that means the open circuit occurs. The diagnosis needs to locate which part is under fault condition by replacing S_0 by S_{A1}, and giving the turn-off single to S_0. In the right part of the converter, S_{A1}, S_{A2}, D_1, S_1, and L_{a34} compose a new asymmetrical half bridge. In the right part asymmetrical half bridge, if the faulty phase can work that proves the left part of converter is under fault condition. By the same method, replacing S_1 by S_{A2}, and giving the turn-off single to S_1; in left part of the converter, S_0, S_{A1}, S_{A2}, D_0, and L_{a12} compose a new asymmetrical half bridge. In the left part asymmetrical half bridge, if the faulty phase can work that proves the right part of the converter is under fault condition. The diagnosis flowchart of the open-circuit fault is shown in Fig. 5.

C. Fault-Tolerance Operation Under Open-Circuit Fault Conditions

When a faulty part is identified in the faulty phase, the fault-tolerance module and main topology combines new topology for faulty phase converter. If the left part of one phase converter is in fault condition, in the fault-tolerance topology, the left part of one-phase converter, including the switching device S_0, diode D_0, and phase winding L_{a12}, is shorted by half bridge S_{A1} and S_{A2} to block faulty part. Fig. 6(a) is the typical example of S_0

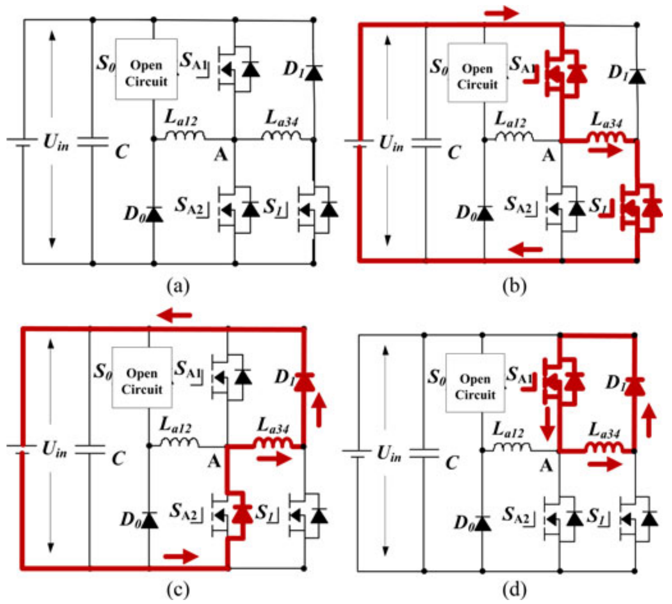

Fig. 6. Fault-tolerance operation topology under open-circuit condition. (a) Upper switch open circuit. (b) Excitation circuit. (c) Energy recycling mode. (d) Freewheeling conduction mode.

under open-circuit condition. When open-circuit fault occurs, the half bridge S_{A1} and S_{A2} is activated to combine with right part converter to form a new fault-tolerance topology. In the new formed fault-tolerance operation topology, when S_{A1} and S_1 conduct, the excitation circuit is shown in Fig. 6(b). Fig. 6(c) presents the energy recycling mode, in which the winding voltage is $-U_{\text{in}}$ to speed up winding demagnetization. Fig. 6(d) shows the freewheeling conduction mode, in which the winding voltage is 0. The working modes of the fault-tolerance converter are the same as a traditional converter**,** except only a half phase winding taking part in working.

The same fault-tolerance operation can be achieved, when D_0 or L_{a12} is faulty. When the right part of the one-phase converter is under open-circuit fault condition, the left part of the one-phase converter and fault-tolerance module can combined to form a new fault-tolerance topology, the same method as Fig. 6.

D. Switching Device and Phase Winding Short-Circuit Fault Diagnosis

When switching device S_0 is short-circuited, the only freewheeling mode is illustrated in Fig. 7(a); when the short-circuit fault of switching device S_1 occurs, the only freewheeling mode is illustrated in Fig. 7(b); Both in Fig. 7(a) and (b) fault condition, the corresponding phase current is always over zero that can be employed in short-circuit fault diagnosis.

When a short-circuit fault is detected, the next step is to locate which switching devices is under fault condition. For example, if S_0 has a short-circuit fault, S_{A1} is enabled by giving drive signals to replace S_0. The right part of the converter and half bridge compose a new asymmetrical half bridge. In the right part asymmetrical half bridge, if the freewheeling current can decrease to zero; the faulty part can be located in S_0; the right part converter and half bridge can form a new converter to achieve fault-tolerance operation that is the same as open circuit. The diagnosis flowchart of the short-circuit fault is shown in Fig. 7(c).

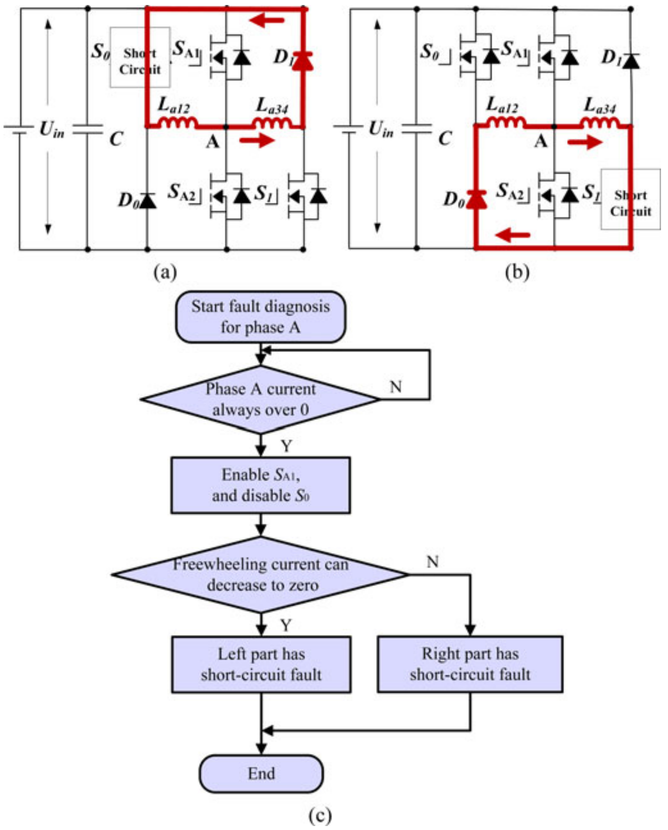

Fig. 7. Diagnosis of switching device short circuits. (a) S_0 short circuit. (b) S_1 short circuit. (c) Diagnosis flowchart of the short-circuit fault.

The left part of the converter and half bridge compose a new asymmetrical half bridge. In the left part asymmetrical half bridge, if the freewheeling current can decrease to zero; the faulty part can be located in S_1; the left part converter and half bridge can form a new converter to achieve fault-tolerance operation that is the same as open circuit.

For instance, when the switching device S_0 is short-circuited, the half-bridge arm and right part converter form new topology. In order to block the faulty part, switching devices S_1 is employed as chopping devices. In excitation and freewheeling state, due to S_{A1} conducting, the both sides of phase winding L_{a12} share the same electric potential that prevent the current forming in L_{a12}; in energy recycle mode, there is no current loop for L_{a12}. Therefore, in the three basic working states, there is no current in phase winding L_{a12}, as presented in Fig. 8(a)∼(c), which proofs left part converter is blocked. Similarly, when switching device S_1 is in short-circuit condition; in order to block the right part converter, S_0 is employed as chopping switching device.

Inner turn short-circuit faults are also the faults to cause the decreasing of phase inductance; but the faulty phase still can operate. The proposed fault-tolerance strategy also can bypass the short-circuited part to stop it from propagating.

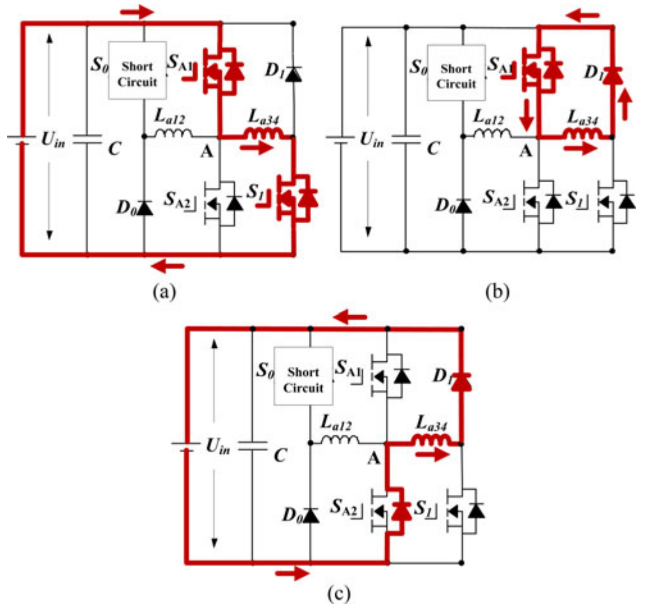

Fig. 8. Fault-tolerance operation under S_0 short circuit condition, (a) Excitation circuit, (b) Freewheeling conduction mode, (c) Energy recycling mode.

III. Fault-Tolerance Operation Control Strategy

After locating a fault part, the corresponding fault-tolerance control strategy is needed to deal with the faulty condition, as described in the following section.

A. Control Schemes for SR Drives

Broadly speaking, there are mainly two methods: current chopping control (CCC) and voltage-PWM control, while many variations exist on the two basic schemes. The drive circuit is assumed to be the same for both schemes. A closed-loop, speed-controlled SRM drive with voltage-PWM regulation scheme and current regulation scheme are shown in Fig. 9. The speed error is processed though a speed controller, such as a proportional integral (PI) controller. The motor speed is obtained from a speed calculator using an encoder to detect the rotor position. The turn-on and turn-off angles are determined by the position detector to control the phase commutation. However, for the system safety, the fault protection part is provided to deal with the drive failure, such as IGBT faults and phase winding faults in the converter.

In SRM driving, the switching sequence is decided by phase conduction sequence. The phase conduction sequence of the SRM adopts a six-step mode as phases A-AB-B-BC-C-CA, as shown in Fig. 9(a). In Fig. 9(b), the phase voltage is the control issue, which is addressed by a voltage controller. The PWM duty cycle is regulated by a PWM generator according to the instantaneous speed, without current regulation. The current waveform has its natural shape at all speeds, as though the supply voltage is chopped down to the value DU_{in} with a duty-cycle *D*. In Fig. 9(c), the phase current is the control issue, which is regulated by a current controller. The instantaneous phase currents, *i*, are measured using the current sensors installed in the phase windings, and fed back to the threshold logic. The current command is added and subtracted from the threshold logic with a hysteresis window, Δ*i*, to obtain the $i_{\max}$ and $i_{\min}$ that determine the switching state of the phase in each turn-on region.

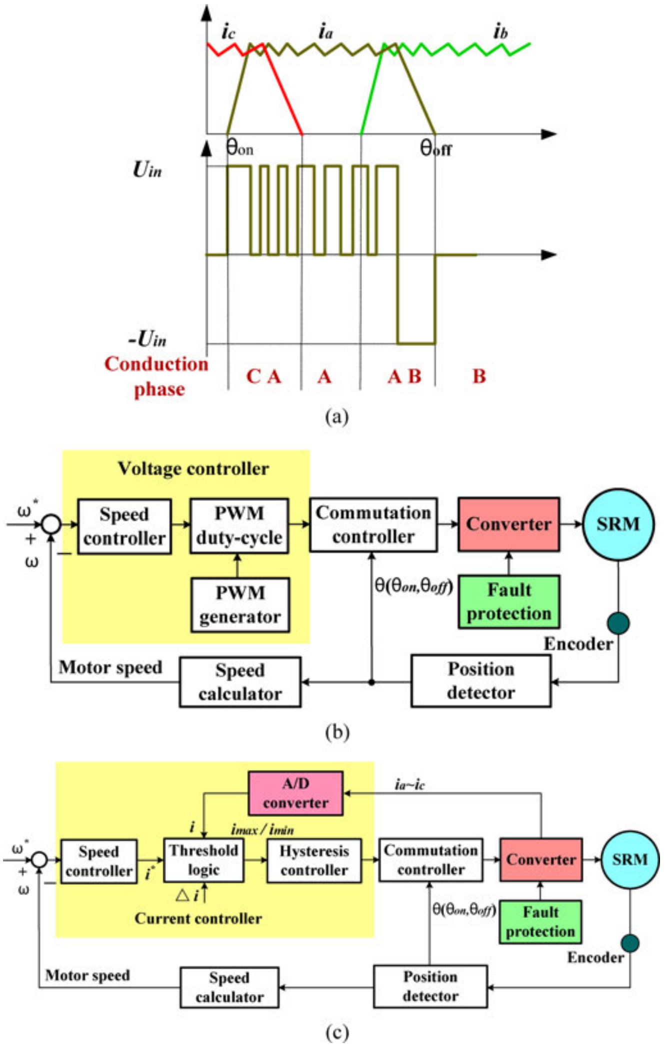

Fig. 9. SRM control strategy. (a) Conduction phase sequence. (b) Diagram of voltage-PWM control system. (c) Diagram of current regulation control system.

B. Characteristics of the Drive Under the Fault-Tolerance Condition

Fig. 10 shows the relationship between phase current and phase inductance. As illustrated in the figure, θ_{on} and θ_{off} are the turn-on and turn-off angles, respectively, i_1 and L_1 are the phase current and phase inductance under the normal conditions, i_2 and L_2 are under the fault-tolerance conditions, and i_4 and i_5 are the phase currents when the turn-on angle is set lagging behind. Fig. 10(a) shows the phase current and phase inductance in the fault-tolerance operation with a half-phase winding, compared to a normal operation; Fig. 10(b) shows the phase current operates in fault-tolerance conditions when the turn-on angle is set lagging behind.

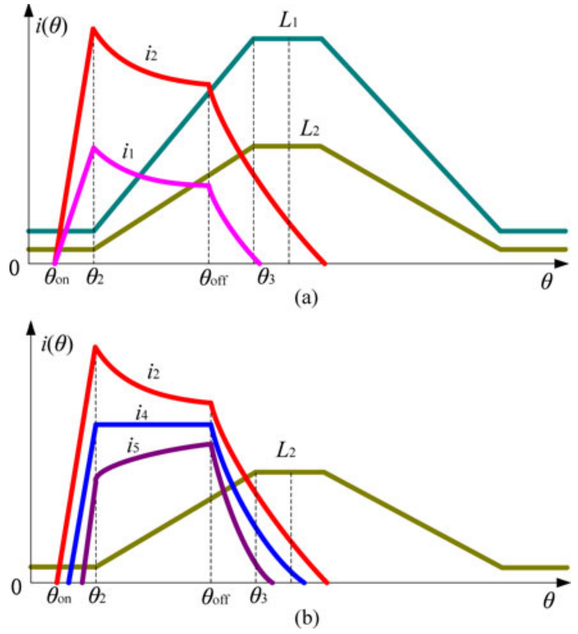

Fig. 10. Relationship between the phase current and phase inductance. (a) Fault-tolerance operation with a half phase winding. (b) Turn-on angle lagging behind.

The phase inductance slope factor in the inductance ascending region is expressed as

$$K_L = \frac{L_{\max} - L_{\min}}{\theta_3 - \theta_2} \tag{1}$$

where $L_{\min}$ and $L_{\max}$ are the minimum and maximum of the phase inductance, and θ_2 and θ_3 are the corresponding rotor position.

In the region of $\theta_{\text{on}} \le \theta < \theta_2$, the phase current is expressed as

$$i(\theta) = \frac{U_{\text{in}}}{\omega_r} \frac{\theta - \theta_{\text{on}}}{L_{\min}} \tag{2}$$

where U_{in} is the bus voltage, and ω_r is the angular velocity. In this region, the phase current goes up quickly, following the current slope factor K_i, given by

$$K_i = \frac{di}{d\theta} = \frac{U_{\text{in}}}{\omega_r L_{\min}} > 0. \tag{3}$$

In the region of $\theta_2 \le \theta < \theta_{\text{off}}$, the phase current is expressed as

$$i(\theta) = \frac{U_{\text{in}}}{\omega_r} \frac{\theta - \theta_{\text{on}}}{L_{\min} + K_L\,(\theta - \theta_2)}. \tag{4}$$

The peak value of the phase current is at the position $\theta = \theta_2$, which is given by

$$i_{\max} = \frac{U_{\text{in}}}{\omega_r} \frac{\theta_2 - \theta_{\text{on}}}{L_{\min}}. \tag{5}$$

The average electromagnetic torque of one phase is given by

$$T_{av} = \frac{N_r}{2\pi} \frac{U_{\text{in}}^2}{\omega_r^2} (\theta_{\text{off}} - \theta_2) \left(\frac{\theta_2 - \theta_{\text{on}}}{L_{\min}} - \frac{1}{2} \frac{\theta_{\text{off}} - \theta_2}{L_{\max} - L_{\min}} \right) \tag{6}$$

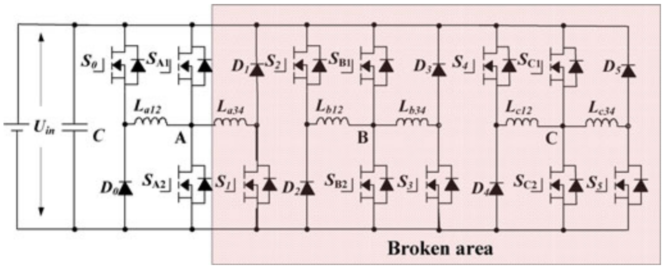

Fig. 11. Extreme faulty operations.

where N_r is the rotor poles.

If the motor system has an open-circuit or short-circuit fault in the converter, the proposed converter will operate with a half part of the fault phase winding, then

$$\begin{cases} L'_{\max} = \dfrac{1}{2} L_{\max} \\[2ex] L'_{\min} = \dfrac{1}{2} L_{\min} \end{cases} \tag{7}$$

where $L'_{\min}$ and $L'_{\max}$ are the minimum and maximum of the faulty phase inductance, respectively.

The phase inductance slope factor in the inductance ascending region in the fault-tolerant operation is as follows:

$$K'_L = \frac{1}{2} \frac{L'_{\max} - L'_{\min}}{\beta_s} = \frac{1}{2} K_L. \tag{8}$$

In the region of $\theta_{\text{on}} \le \theta < \theta_2$, the phase current slope in fault-tolerant operation is as follows:

$$K'_i = \left(\frac{di}{d\theta}\right)' = \frac{U_{\text{in}}}{\omega_r \frac{1}{2} L_{\min}} = \frac{2U_{\text{in}}}{\omega_r L_{\min}} = 2K_i. \tag{9}$$

The peak value of the phase current at the position $\theta = \theta_2$, in fault-tolerant operation, is

$$i'_{\max} = \frac{U_{\text{in}}}{\omega_r} \frac{\theta_2 - \theta_{\text{on}}}{\frac{1}{2} L_{\min}} = \frac{U_{\text{in}}}{\omega_r} \frac{2(\theta_2 - \theta_{\text{on}})}{L_{\min}} = 2 i_{\max}. \tag{10}$$

The average electromagnetic torque of the failure phase is given by

$$\begin{aligned} T'_{\text{av}} = {} & \frac{N_r}{2\pi} \frac{U_{\text{in}}^2}{\omega_r^2} (\theta_{\text{off}} - \theta_2) \left(\frac{\theta_2 - \theta_{\text{on}}}{\frac{1}{2} L_{\min}} \right. \\ & \left. - \frac{1}{2} \cdot \frac{\theta_{\text{off}} - \theta_2}{\frac{1}{2} L_{\max} - \frac{1}{2} L_{\min}} \right) = 2T_{\text{av}}. \end{aligned} \tag{11}$$

According to (10) and (11), the peak value of the phase current, and the average electromagnetic torque of the failure phase are double of the normal value when working in fault-tolerant operation. However, in a closed-loop system, the total average electromagnetic torque is the same as that in the normal state, due to a constant load.

When an open-circuit fault of the drive happens, conventionally, the system still works in the phase absence operation to ensure the continued working ability in a closed-loop system. However, the currents of other normal phases will be larger than the previous one to compensate the torque output, due to the adjustment of the speed controller. The unbalanced phase current

TABLE I
PROPOSED FAULT-TOLERANCE TOPOLOGY COMPARING WITH OTHER FAULT-TOLERANCE METHODS

	Proposed method	Traditional SRM system [13]	Specially designed motor [25][27]	Fault tolerance topology	
				Paper [29]	Paper [28]
Motor structure	Traditional SRM	Traditional SRM	Special design	Special design	Traditional SRM
Fault diagnosis	Easy	Complicated	N/A	Easy	N/A
Fault tolerance	Achievable without phase absence	Achievable with phase absence	Achievable with phase absence	Achievable without phase absence	Achievable with phase absence
Modular structure	Yes	Yes	Yes	Yes	No
Cost	Medium	Low	High	High	Medium
Operation at extreme faults	Achievable	No	Achievable	Achievable	No

increases the torque ripple and the load capacity also is reduced considerably. When the short-circuit fault of the drive happens, the demagnetization current cannot decrease to zero due to a zero-voltage loop, which causes phase current more unbalanced and obviously increases the torque ripple.

Considering the proposed fault-tolerance scheme in the CCC system, a half of the failure phase still can be put into use to ensure the torque output. Since the phase current is the control target, it will be regulated to the same reference compared to the normal one, even though a half of the failure phase is removed. In voltage-PWM control strategy, the phase voltage is the control target. The imposed voltage on each phase is the same, no matter the phase winding works in a whole part or half part. In order to reduce the unbalanced phase current further in voltage-PWM system, the turn-on angle of the failure phase can be adjusted lagging behind to reduce the increased phase current in the failure winding, as illustrated in Fig. 10(b). Hence, the proposed drive topology can be used to compensate the current and torque, and reduce the torque ripple to improve the drive performance in fault conditions.

C. Comparison of the Proposed Fault-Tolerance Operation With Other Strategies

In the traditional fault-tolerance strategy, the defective-phase-operation also can be achieved. In a worse fault condition, such as all upper switching devices (S_0, S_2, S_4) are broken, the SRM cannot work. By the proposed fault-tolerance strategy, the topology still can operate under extreme faulty conditions. The proposed topology can support one of switching devices in each phase converter under fault condition.

In extreme faulty operation condition, only one switching of main driving topology is healthy. The proposed fault-tolerance strategy still can sustain the SRM operation. As the illustrated in Fig. 11, only left part of phase L_a converter is healthy; the S_0, S_{A1}, S_{A2}, and D_0 compose a new topology that can maintain operation of the SRM under light load condition.

A comparison of the proposed fault-tolerance topology and existing fault-tolerance methods is illustrated in Table I. It can be seen that the proposed method has a better overall performance, which will be proved in the following sections.

Fig. 12. Traditional current sensor placement strategy.

D. Design Procedure

There are three basic steps in the system design procedure.

1) Developing key parameters and application specifications, including rated power, torque, supply voltage, rated speed, speed range, and efficiency, design switched reluctance motor [3].
2) Building SRM simulation models in Ansoft to check the electromagnetic performance, and optimizing key parameters.
3) Converter design in relation to SRM working condition. By building SRM models and converter models in MATLAB/Simulink, The starting, braking, rated power operation, and over power operation are simulated to support for switching device selection. The fault-tolerance topology chooses the same switching devices with the main driving topology.

IV. PHASE CURRENT SENSOR PLACEMENT STRATEGY

The phase current is the main source of information for fault-diagnosis and fault-tolerance operation. In the proposed fault-tolerance topology, the current sensor placement strategy is studied considering the cost and modular structure.

A. Single Current Sensor Placement Strategy

Current sensors are expensive and need extra A/D channels to transfer analog signal to digital signals for the controller so that the system cost is increased. The single current sensor is one of the best choices. The traditional current sensor strategy is illustrated in Fig. 12; there are four candidate placement positions, but none of them can give the phase current signal both under left part and right part phase converter fault condition.

Fig. 13(a) is the proposed current sensor placement strategy. The number of turns in both sides from the point A is the same. In normal condition, there is no current passing point A, as

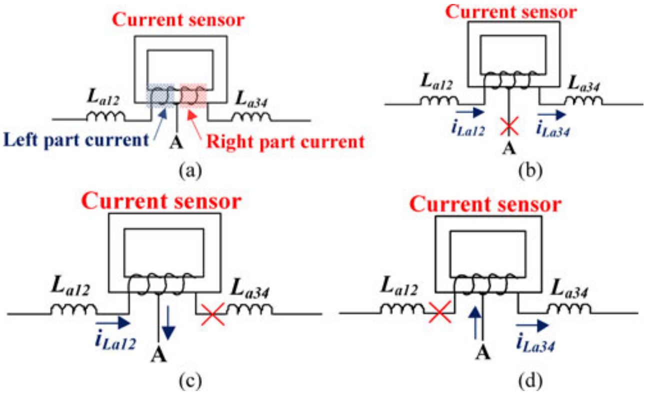

Fig. 13. Proposed single current placement strategy. (a) Proposed single current sensor placement strategy. (b) Normal condition. (c) Right part fault condition. (d) Left part fault condition.

shown in Fig. 13(b). The current sensor output is the sum of i_{La12} and i_{La34}. When the right part of the phase converter is fault, by the fault-tolerance operation, the right part is shorted by the half-bridge switching devices; the output of the current sensor is i_{La12}, as shown in Fig. 13(c). When the left part of the phase converter is fault, by the fault-tolerance operation, the left part is shorted by the half-bridge switching devices; the output of the current sensor is i_{La34}, as illustrated in Fig. 13(d). The output of current sensor signal magnification times is only half the normal condition. Compared with the traditional sensor placement strategy, the proposed method can give the phase current information at fault-tolerance operation condition.

B. Dual Current Sensor Placement Strategy

Fig. 12 shows the current placement strategy. Although the number of current sensors is decreased, the output of sensor signal magnification times is also changed when fault occurs that may be inconvenient for the controller. Furthermore, the Fig. 13 strategy does not have the characteristics of modulation.

Dual sensors can give the separate signals of both left part and right part of the phase winding current. Fig. 14(a) is the basic structure of the dual current placement strategy. On the whole structure, Fig. 14(a) does not have the characteristics of modular. Because current commercial drive mode for the SRM has combined one current sensor for each phase and half-bridge drive topology as the standard configuration. Fig. 14(b) gives another solution. The current placement strategy in main drive topology is the same as usual; the other current sensor is in fault-tolerance part. In a normal condition, the current sensors CS_A, CS_B, and CS_C give the phase current information. When fault occurs, the current sensors CS_{A1}, CS_{B1} and CS_{C1} give the phase current information in fault-tolerance operation. Because the main drive topology and its current sensor compose a relative independent system; the fault-tolerance topology and its corresponding current sensors also have relative independence. Due to the modular and independence characteristics, the proposed fault-tolerance strategy can be used in the current SRM system without any hardware change.

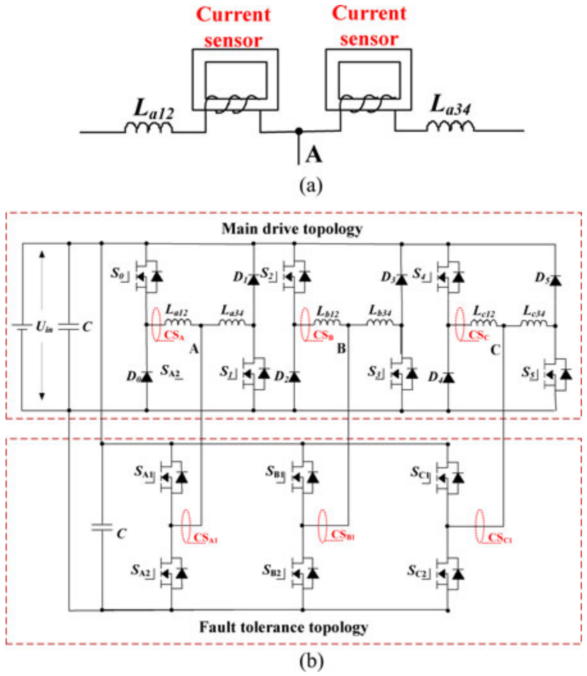

Fig. 14. Dual current placement strategy. (a) Dual current sensor placement strategy. (b) Proposed dual current sensor placement strategy.

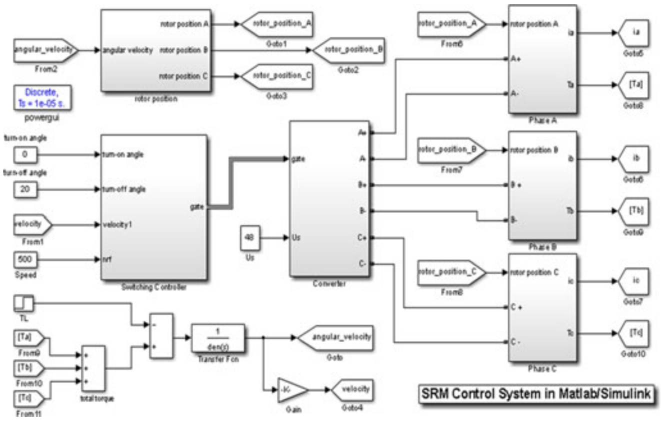

Fig. 15. SRM control system in MATLAB/Simulink.

V. Simulation and Experiment

In order to validate the proposed fault-tolerance topology, a 750-W 12/8 SRM is employed to be modeled in the MATLAB/Simulation. The SRM control system is developed in MATLAB/Simulink, as shown in Fig. 15. The rotor position is obtained by a position calculator from the angular velocity. The converter is built by using the models in the SimPowerSystems. The velocity is calculated according to the total torque exporting from the phase model and the load torque. The switching controller is used to give the gate signals according to the given speed, instantaneous speed, turn-on angle, and turn-off angle. Every phase current and torque can be observed directly in different simulation conditions.

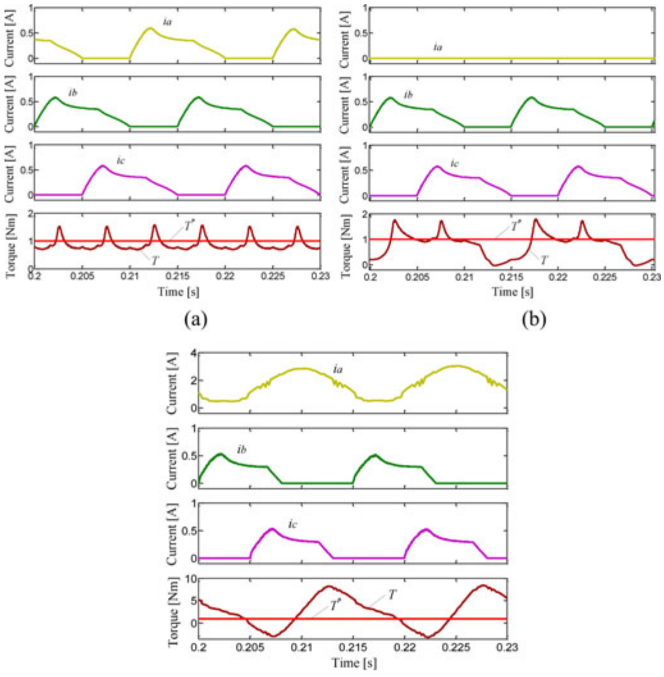

(a) (b)

(c)

Fig. 16. Simulation results of voltage-PWM control mode under normal and fault conditions. (a) Normal condition. (b) Open fault. (c) Short fault.

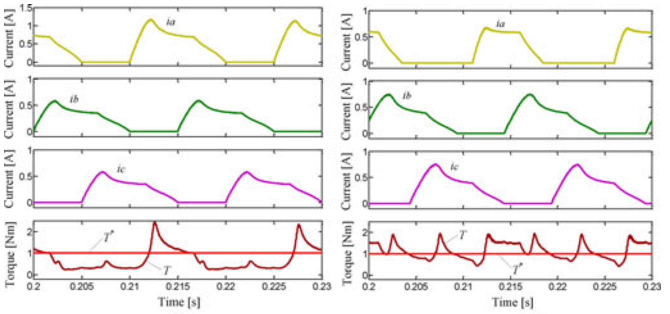

(a) (b)

Fig. 17. Simulation results of voltage-PWM control mode with fault-tolerance topology under fault conditions. (a) Turn-on angle is 0° for phase *A*. (b) Turn-on angle is 5° for phase *A*.

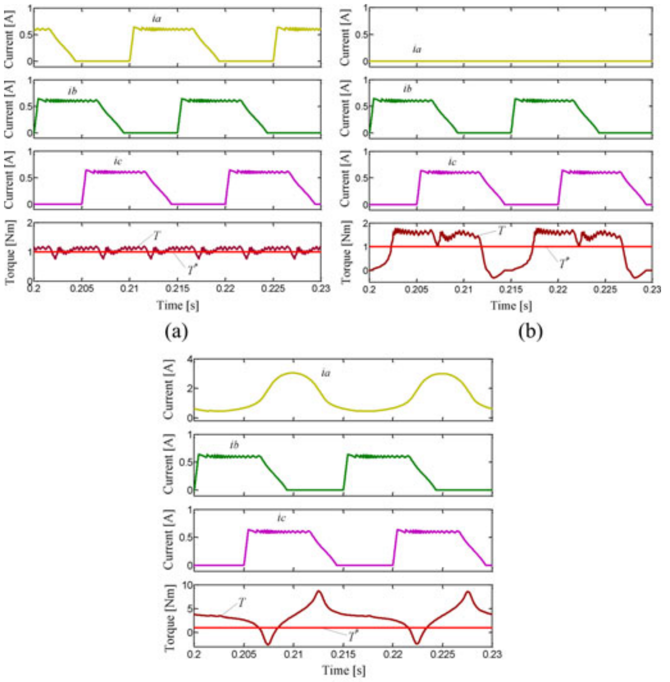

(a) (b)

(c)

Fig. 18. Simulation results of current regulation control mode with fault-tolerance topology under fault conditions. (a) Normal. (b) Open fault. (c) Short fault.

Fig. 16 shows the voltage-PWM control mode at 500 r/min under normal and fault conditions, respectively. The turn-on angle is set to 0° and the turn-off angle to 20°. The load torque is set to 1 N·m. In the simulation results, i_a, i_b, and i_c represent for phase *A*, *B*, and *C* current, respectively. *T* and T^* represent for the instantaneous torque and given load torque, respectively. When the drive operates in the normal state, the three phase currents have the same shape with 15° phase-shift compare to each other, and the total torque is the sum of three phase torque, as shown in Fig. 16(a). Due to the independence of each phase leg, the fault phase will not affect the other normal phase. For example of phase *A*, when an open-fault happens, phase *A* current declines to zero, and the torque is only the sum of phase *B* and *C* torque. In a closed-loop system, when the open-fault happens, the other two phase currents are excited to be larger than the previous one by increasing the PWM duty cycle, to compensate the absent phase torque. However, the torque ripple gets larger than that in normal conditions, as shown in Fig. 16(b). When a short-fault happens in upper-switch of phase *A*, the phase voltage cannot be regulated in phase turn-on region, and the demagnetization current also cannot flow to power supply in the phase turn-off region, as shown in Fig. 16(c). In this fault state, phase A current is obviously larger than the normal phase, causing the torque ripple.

Fig. 17 shows the voltage-PWM control mode at 500 r/min with fault-tolerance topology under fault condition. The additional three-phase half bridge is put into use, no matter an open-fault or short fault is detected. As illustrated in Fig. 17(a), the current slope and peak value of phase A in the initial conduction region are double of the normal value, based on the aforementioned analysis. Despite using the fault-tolerant topology, the torque ripple and unbalanced degree of the phase current are still large. In order to reduce them effectively, a fault-tolerant scheme that lagging the turn-on angle of the fault phase is carried out, as shown in Fig. 17(b). The turn-on angle is set to 5° for phase A, and the torque ripple is clearly reduced compared to Fig. 17(a).

Fig. 18 shows the current regulation control mode under normal and faulty conditions, respectively. As shown in Fig. 18(a), the torque ripple is smaller than that of voltage-PWM control mode in normal condition. The results under open- and short-fault conditions are similar to the voltage-PWM control mode, as shown in Fig. 18(b) and (c). Fig. 19 shows the fault-tolerance results in current regulation control mode at 500 r/min. In a

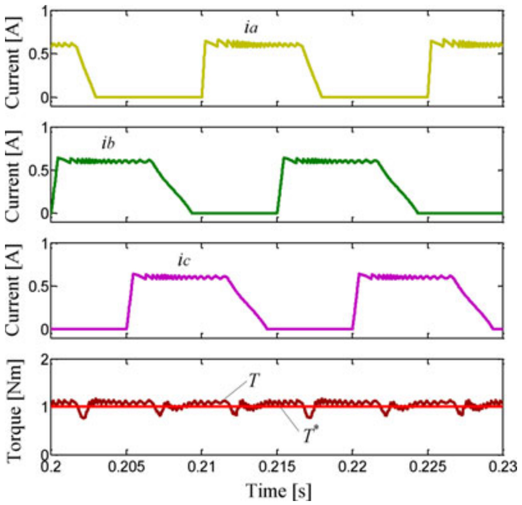

Fig. 19. Simulation results of current regulation control mode with fault-tolerance topology under fault conditions.

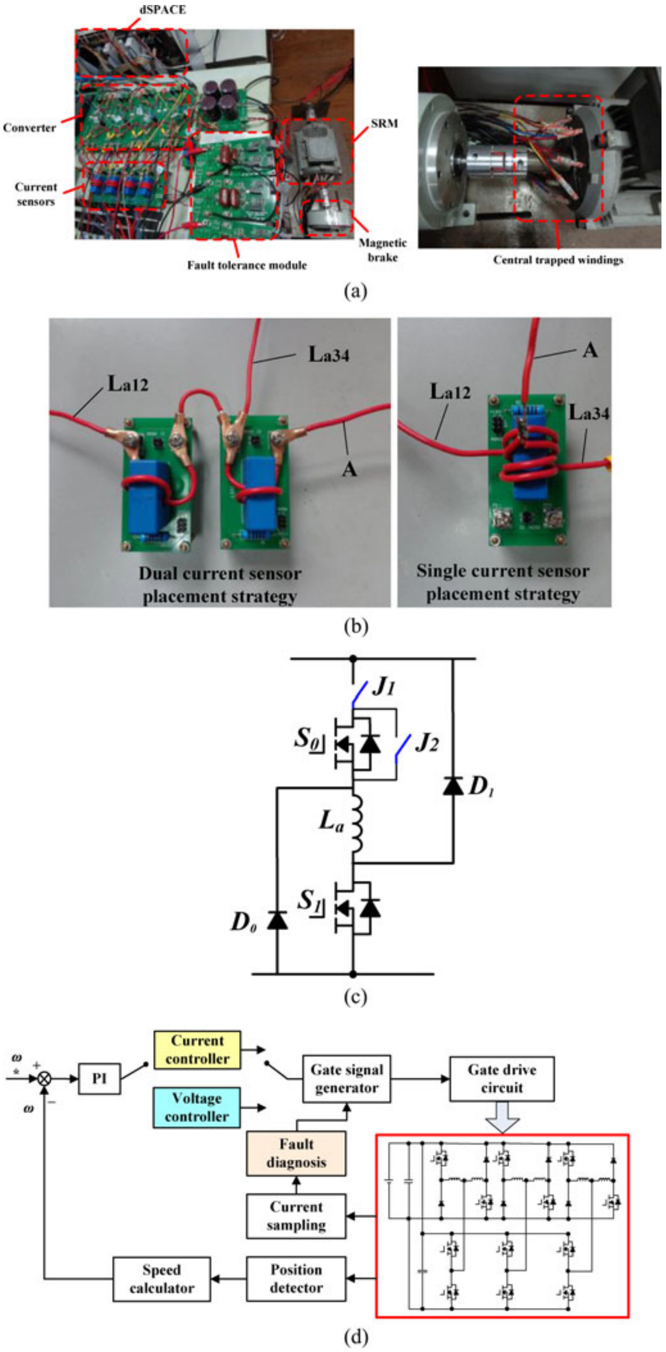

(a)

(b)

(c)

(d)

Fig. 20. Experimental setup and the control system. (a) Experimental setup. (b) Details of the two current sensors placement method. (c) Generation of faults by J_1 and J_2, (d) Diagram of the fault-tolerance control system.

current regulation control system, phase current is the control target, and it is regulated to the same reference compared to the normal one. The only differences are the current slope. The torque ripple is effectively reduced to the normal one compared to Fig. 18(a), if the fault-tolerance topology is adopted.

To verify the effectiveness of the proposed scheme experimentally, an experimental rig for testing a 750-W SRM prototype is set up, as shown in Fig. 20(a). Photographs of the employed current sensors are shown in Fig. 20(b). Two air switches are adopted to emulate open-circuit and short-circuit faults, as shown in Fig. 20(c), where J_1 is used to achieve an open-circuit fault and J_2, a short-circuit fault. The main motor parameters are illustrated in Table II. Fig. 20(d) shows the fault-tolerance control system diagram with the closed-loop speed regulation capability. As illustrated in the figure, a PI controller is used to regulate the motor speed, and the proportional gain and integral gain are 0.05 and 0.5, respectively. The current controller and voltage controller are utilized to generate the drive signals to control the motor drive in different operation modes. The position detector and speed calculator are used to give the instantaneous speed for feedback control. The current sampling and fault-diagnosis schemes are employed to control the gate signals for the fault-tolerance topology to operate under faulted conditions.

The type of the used MOFESTs is FDA59N30 from Fairchild Inc; and diodes are IDW75E60 from Infineon Technologies. Three current sensors (LA55Ps) are used to measure the phase currents. An incremental encoder with 1000 lines is used to measure the rotor position. A dSPACE 1006 control board is employed to implement the control scheme, with its control diagram shown in Fig. 21(a) and flowcharts in Fig. 21(b) and (c). A magnetic brake acts as the load with a torque of 1 N·m. The dc-link voltage is fixed to 48 V. Two air switches are adopted to generate open-circuit and short-circuit faults. The torque observed in the oscilloscope is obtained online by using the real-time phase currents and rotor position to look up for the torque value in a 3-D torque table that includes the $T - i - \theta$ characteristics [33], [34]. The torque data in the lookup table are measured by using a rotor clamping device when supplying different steady currents to the motor windings in a rotor position that changes step by step. The output torque in the experimental waveforms is observed though a D/A converter.

The turn-on and turn-off angles are set to 0° and 20°. In voltage-PWM control system with fault-tolerance topology, the turn-on angle is set to 5° to improve the phase current balance

TABLE II
MOTOR PARAMETERS

Parameters	Value
Phase number	3
Stator poles	12
Rotor poles	8
Rated speed (r/min)	1500
Rated power (W)	750
Phase resistor (Ω)	3.01
Minimum phase inductance (mH)	27.2
Maximum phase inductance (mH)	256.7
Rotor outer diameter (mm)	55
Rotor inner diameter (mm)	30
Stator outer diameter (mm)	102.5
Stator inner diameter (mm)	55.5
Core length (mm)	80
Stator arc angle (deg)	14
Rotor arc angle (deg)	16

for the fault-tolerance performance when the short-fault occurs. Figs. 22–25 present the experimental results at 500 r/min, where i_a, i_b, and i_c are the phase currents for phase *A*, *B*, and *C*, respectively; T^* and T are the given load torque and instantaneous torque, which show a good agreement with the simulation results. Fig. 22 presents the typical voltage-PWM control model waveforms of the SRM under normal, open-circuit fault, and short-circuit fault conditions. In a normal condition, three phases have the same current amplitude and shape. In an open-circuit faulty condition, there is no current in the faulty phase. In a short-circuit faulty condition, the faulty phase current cannot decrease to zero. The experiment results have agreed well with the analytical study in Section II. Fig. 23 verifies the control strategy under fault condition. By controlling the turn-on angle of phase *A*, the output torque ripple can be decreased obviously. Fig. 24 shows the typical waveforms for the current regulation control model under normal, open fault, and short fault condition. In an open-circuit faulty condition, there is no current in the faulty phase, while in a short-circuit faulty condition, as theory analysis, the fault phase current cannot decrease to zero. The experiment results also verify the theory analysis in Section II. Under these fault-tolerance operation conditions, the faulty phase current and output torque with the proposed method can follow the reference values faithfully, as shown in Fig. 25. This is also the case in reducing the torque ripple and the imbalance between phase currents for conventional converters with either open-circuit or short-circuits faults.

Fig. 26 shows the fault-tolerance operation at 500 r/min and 5-N·m load in CCC and PWM systems, respectively. The system can still be stable when operating at large load and make up for the missing output torque of the fault phase. Fig. 27 shows the operation of the developed system during acceleration and at high speeds with a 1-N·m load. As illustrated in Fig. 27(a), the speed follows the given value well during the continuous acceleration progress. In Fig. 27(b), the system is still stable when it is operated at 1500 r/min, which shows a good stability at high speed.

Fig. 28 shows the fault-tolerance operation with only a half phase winding at 500 r/min and 1-N·m load in CCC and PWM systems, respectively. The system can still operate with only a half phase winding at light load. Fig. 29 shows the fault-tolerance operation with only a half phase winding during acceleration and load increasing. The speed still follows the given speed well no matter during acceleration and in steady state. However, in Fig. 29(b), when the load increases from 1 to 3 N·m, the speed is reduced due to the insufficient load ability. Hence, in the extreme faulty conditions, the proposed fault-tolerance scheme can still operate at light loads.

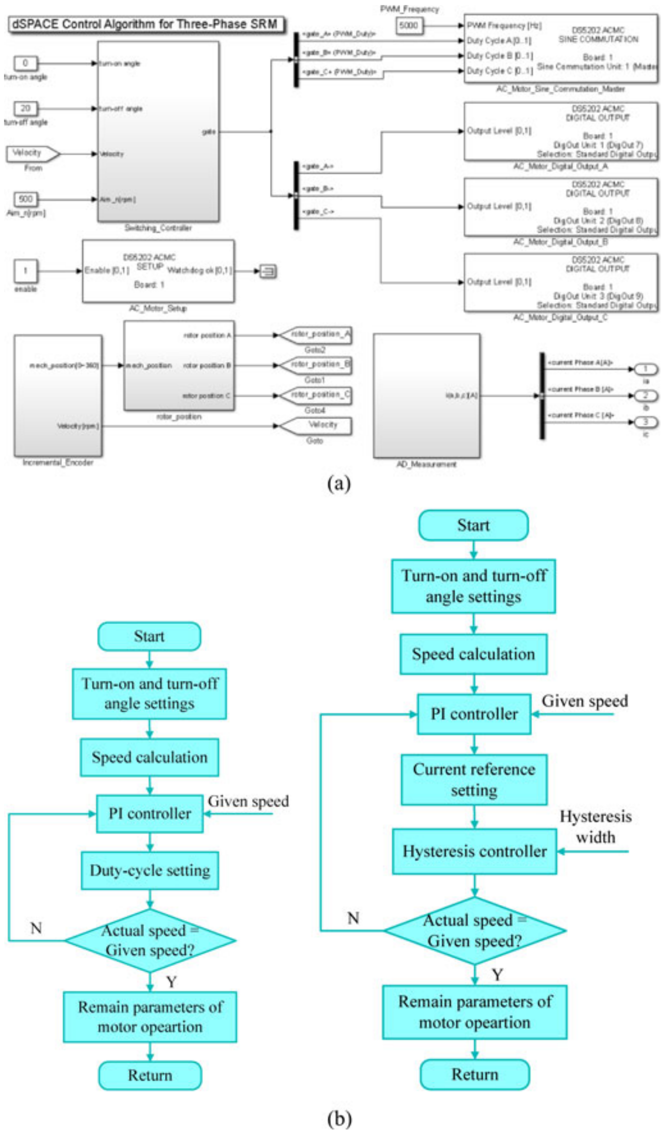

Fig. 21. dSPACE control algorithm. (a) dSPACE control diagram. (b) Flowchart of algorithm for voltage-PWM control. (c) Flowchart of algorithm for current regulation control.

VI. CONCLUSION

In this paper, a central-tapped node linked modular fault-tolerance topology is proposed for SRM-based EV applications, based on the axial symmetrical structure of the phase converter. The main contributions of this paper are: 1) a novel

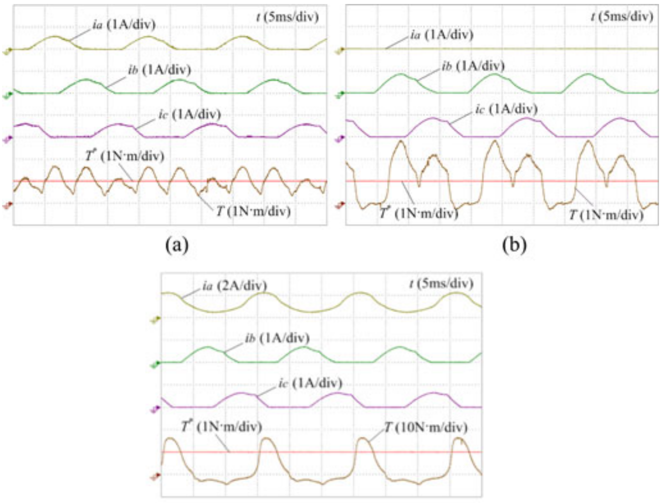

(a) (b) (c)

Fig. 22. Experimental results of voltage-PWM control mode under normal and fault conditions. (a) Normal. (b) Open fault. (c) Short fault.

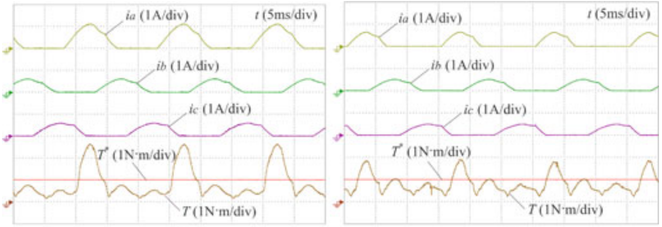

(a) (b)

Fig. 23. Experimental results of voltage-PWM control mode with fault-tolerance topology under fault conditions. (a) Turn-on angle is 0° for phase *A*. (b) Turn-on angle is 5° for phase *A*.

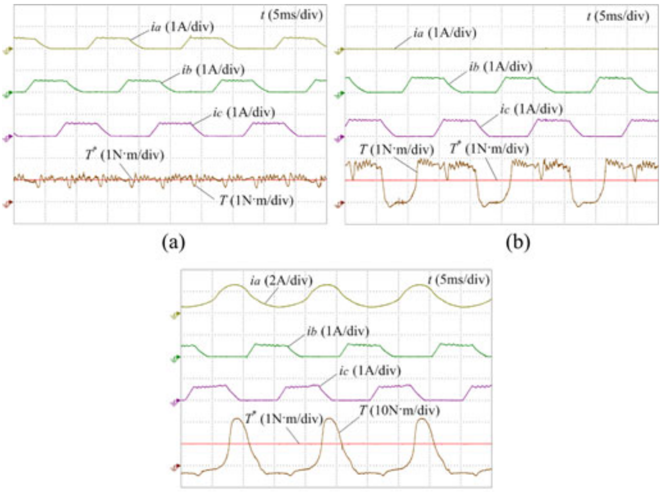

(a) (b) (c)

Fig. 24. Experimental results of current regulation control mode with fault-tolerance topology under fault conditions. (a) Normal. (b) Open fault. (c) Short fault.

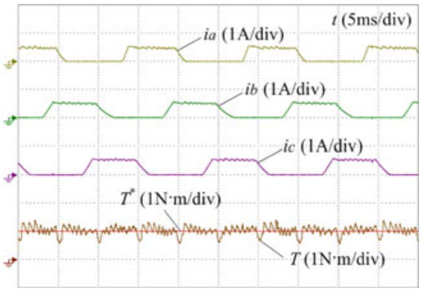

Fig. 25. Experimental results of current regulation control mode with fault-tolerance topology under fault conditions.

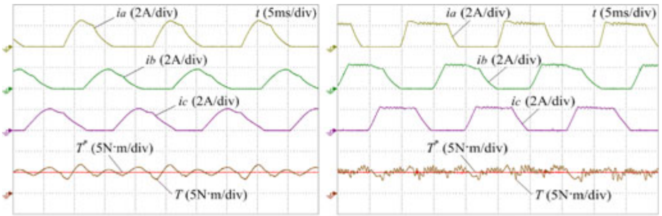

(a) (b)

Fig. 26. Experimental results of fault-tolerance operation under the high load. (a) PWM system. (b) CCC system.

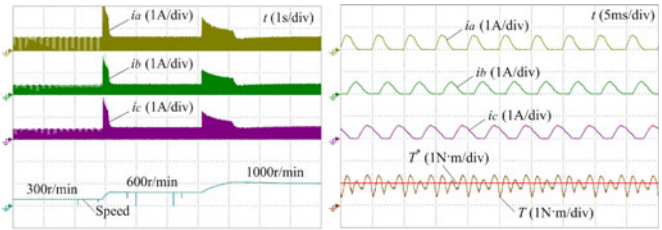

(a) (b)

Fig. 27. Experimental results of fault-tolerant operation during acceleration and at high-speed operation. (a) Acceleration. (b) High-speed operation.

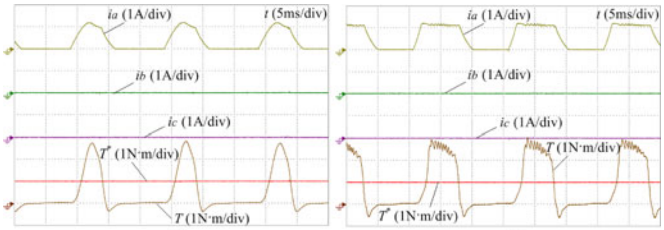

(a) (b)

Fig. 28. Experimental results of fault-tolerance operation with only a half phase winding in the extreme faulty condition at steady-state operation. (a) CCC system. (b) PWM system.

fault-tolerance SRM topology is developed with a modular structure; 2) fault diagnosis and the corresponding fault-tolerance architecture are proposed to achieve convenient fault diagnosis and improve fault-tolerance performance of the SRM; and 3) two current sensor placement strategies are also developed to achieve low cost and modular structure.

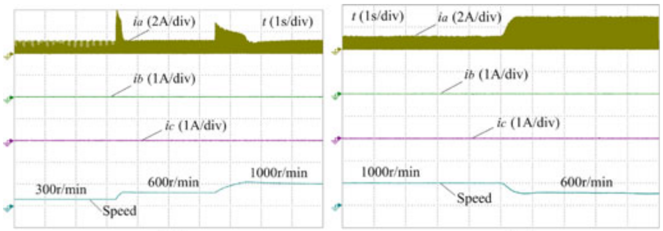

(a) (b)

Fig. 29. Experimental results of fault-tolerance operation with only a half phase winding during acceleration and load increasing. (a) Acceleration. (b) Load increasing.

By combining the modular SRM fault-tolerance structure with the central tapped node, the fault in the phase converter can be diagnosed easily; the faulty part can be blocked by the fault-tolerance topology to achieve fault-tolerance operation. Furthermore, the proposed system is in an idle condition when the SRM drive is healthy. The modular topology can be added to the traditional SRM drives without much change to the circuitry. The proposed current sensor placement strategy offers a low-cost and modular solution to typical power switch faults. The developed technologies can be applied to high-reliability drive applications such as electric vehicles, ships, and aerospace.

REFERENCES

[1] B. K. Bose, “Global energy scenario and impact of power electronics in 21st century,” *IEEE Trans. Ind. Electron.*, vol. 60, no. 7, pp. 2638–2651, Jul. 2013.

[2] Y. Hu, X. Song, W. Cao, and B. Ji, “New SR drive with integrated charging capacity for plug-in hybrid electric vehicles (PHEVs),” *IEEE Trans. Ind. Electron.*, vol. 61, no. 10, pp. 5722–5731, Oct. 2014.

[3] T. J. E. Miller, *Switched Reluctance Motors and Their Control*, London, U.K.: Magna Physics Publishing and Oxford Science, 1993, pp. 3–25.

[4] J. Liang, D. H. Lee, G. Xu, and J. W. Ahn, “Analysis of passive boost power converter for three-phase SR drive,” *IEEE Trans. Ind. Electron.*, vol. 57, no. 9, pp. 2961–2971, Sep. 2010.

[5] D. H. Lee, T. H. Pham, and J. W. Ahn, “Design and operation characteristics of four-two pole high-speed SRM for torque ripple reduction,” *IEEE Trans. Ind. Electron.*, vol. 60, no. 9, pp. 3637–3643, Sep. 2013.

[6] L. Shen, J. Wu, and S. Yang, “Initial position estimation in SRM using bootstrap circuit without predefined inductance parameters,” *IEEE Trans. Power Electron.*, vol. 26, no. 9, pp. 2449–2456, Sep. 2011.

[7] A. G. Jack, B. C. Mecrow, and J. A. Haylock, “A comparative study of permanent magnet and switched reluctance motors for high-performance fault-tolerant applications,” *IEEE Trans. Ind. Appl.*, vol. 32, no. 4, pp. 889–895, Jul./Aug. 1996.

[8] S. Gopalakrishnan, A. M. Omekanda, and B. Lequesne, “Classification and remediation of electrical faults in the switched reluctance drive,” *IEEE Trans. Ind. Appl.*, vol. 42, no. 2, pp. 479–486, Mar/Apr. 2006.

[9] B. Ji, V. Pickert, W. Cao, and B. Zahawi, “*In situ* diagnostics and prognostics of wire bonding faults in IGBT modules for electric vehicle drives,” *IEEE Trans. Power Electron.*, vol. 28, no. 12, pp. 5568–5577, Dec. 2013.

[10] H. Torkaman, E. Afjei, and P. Yadegari, “Static, dynamic, and mixed eccentricity faults diagnosis in switched reluctance motors using transient finite element method and experiments,” *IEEE Trans. Magn.*, vol. 48, no. 8, pp. 2254–2264, Aug. 2012.

[11] N. S. Gameiro, and A. J. Marques Cardoso, “A new method for power converter fault diagnosis in SRM drives,” *IEEE Trans. Ind. Appl.*, vol. 48, no. 2, pp. 653–662, Mar./Apr. 2012.

[12] C. Hao and L. Shengli, “Fault diagnosis digital method for power transistors in power converters of switched reluctance motors,” *IEEE Trans. Ind. Electron.*, vol. 60, no. 2, pp. 749–763, Feb. 2013.

[13] J. F. Marques, J. O. Estima, N. S. Gameiro, and A. M. Cardoso, “A new diagnostic technique for real-time diagnosis of power converter faults in switched reluctance motor drives,” *IEEE Trans. Ind. Appl.*, vol. 50, no. 3, pp. 1854–1860, May/Jun. 2014.

[14] N. S. Gameiro and A. J. M. Cardoso, “Fault tolerant control strategy of SRM drives,” in *Proc. IEEE Int. Symp. Power Electron., Electr. Drives, Autom. Motion*, Ischia, Italy, Jun. 2008, pp. 301–306.

[15] A. A. Arkadan, P. Du, M. Sidani, and M. Bouji, “Performance prediction of SRM drive systems under normal and fault operating conditions using GA-based ANN method,” *IEEE Trans. Magn.*, vol. 36, no. 4, pp. 1945–1949, Jul. 2000.

[16] M. Bouji, A. A. Arkadan, and T. Ericsen, “Fuzzy inference system for the characterization of SRM drives under normal and fault conditions,” *IEEE Trans. Magn.*, vol. 37, pp. 3745–3748, Sep. 2001.

[17] A. A. Arkadan and B. W. Kielgas, “Switched reluctance motor drive systems dynamic performance prediction under internal and external fault conditions,” *IEEE Trans. Energy Convers.*, vol. 9, no. 1, pp. 45–52, Mar. 1994.

[18] B. Lequesne, S. Gopalakrishnan, and A. M. Omekanda, “Winding short circuits in the switched reluctance drive,” *IEEE Trans. Ind. Appl.*, vol. 41, no. 5, pp. 1178–1184, Sep/Oct. 2005.

[19] H. Torkaman and E. Afjei, “Comprehensive detection of eccentricity fault in switched reluctance machines using high-frequency pulse injection,” *IEEE Trans. Power Electron.*, vol. 28, no. 3, pp. 1382–1390, Mar. 2013.

[20] L. A. Belfore, II and A. Arkadan, “A methodology for characterizing fault tolerant switched reluctance motors using neurogenetically derived models,” *IEEE Trans. Energy Convers.*, vol. 17, no. 3, pp. 380–384, Sep. 2002.

[21] S. Mir, M. S. Islam, T. Sebastian, and I. Husain, “Fault-tolerant switched reluctance motor drive using adaptive fuzzy logic controller,” *IEEE Trans. Power Electron.*, vol. 19, no. 2, pp. 289–295, Mar. 2004.

[22] M. D. Hennen, M. Niessen, C. Heyers, H. J. Brauer, and R. W. De Doncker, “Development and control of an integrated and distributed inverter for a fault tolerant five-phase switched reluctance traction drive,” *IEEE Trans. Power Electron.*, vol. 27, no. 2, pp. 547–554, Feb. 2012.

[23] A. Labak and N. C. Kar, “Designing and prototyping a novel five-phase pancake-shaped axial-flux SRM for electric vehicle application through dynamic FEA incorporating flux-tube modeling,” *IEEE Trans. Ind. Appl.*, vol. 49, no. 3, pp. 1276–1288, May/Jun. 2013.

[24] W. Ding, Y. Liu, and Y. Hu, “Performance evaluation of a fault-tolerant decoupled dual-channel switched reluctance motor drive under open-circuits,” *IET Electric Power Appl.*, vol. 8, no. 4, pp. 117–130, Apr. 2014.

[25] M. Ruba, I.-A. Viorel, and L. Szabo, x, “Modular stator switched reluctance motor for fault tolerant drive systems,” *IET Electric Power Appl.*, vol. 7, no. 3, pp. 159–169, Mar. 2013.

[26] H. Torkaman, E. Afjei, and M. S. Toulabi, “New double-layer-per-phase isolated switched reluctance motor: concept, numerical analysis, and experimental confirmation,” *IEEE Trans. Ind. Electron.*, vol. 59, no. 2, pp. 830–838, Feb. 2012.

[27] L. Szabo and M. Ruba, “Segmental stator switched seluctance machine for safety-critical applications,” *IEEE Trans. Ind. Appl.*, vol. 48, no. 6, pp. 2223–2229, Nov./Dec. 2012.

[28] N. S. Gameiro and A. J. M. Cardoso, “Fault tolerant power converter for switched reluctance drives,” in *Proc. 18th Int. Conf. Electr. Machines*, Algarve, Portugal, Sep. 2008, pp. 1–6.

[29] M. Ruba, C. Oprea, and L. Szabó, “Comparative study on switched reluctance machine based fault-tolerant electrical drive systems,” in *Proc. IEEE Int. Conf. Electric Machines Drives*, Miami, USA, May 2009, pp. 987–992.

[30] W. Wang and B. Fahimi, “Fault resilient strategies for position sensorless methods of switched reluctance motors under single and multiphase fault,” *IEEE J. Emerg. Sel. Topics Power Electron.*, vol. 2, no. 2, pp. 190–200, Jun. 2014.

[31] A. C. Oliveira, C. B. Jacobina, A. M. N. Lima, and F. Salvadori, “Startup and fault tolerance of the SRM drive with three-phase bridge inverter,” in *Proc. IEEE Power Electron. Spec. Conf.*, Recife, Brazil, Jun. 2005, pp. 714–719.

[32] L. Xu, D. Zhao, C. Zhang, and R. P. Ge, “Research on fault analysis and fault-tolerant control of valve electric actuator system based on SRM,” in *Proc. Int. Symp. Comput. Intell. Design*, Hangzhou, China, Oct. 2012, pp. 389–393.

[33] D. H. Lee, J. Liang, Z. G. Lee, and J. W. Ahn, “A simple nonlinear logical torque sharing function for low-torque ripple SR drive,” *IEEE Trans. Ind. Electron.*, vol. 56, no. 8, pp. 3021–3028, Aug. 2009.

[34] V. P. Vujic, “Minimization of torque ripple and copper losses in switched reluctance drive,” *IEEE Trans. Power Electron.*, vol. 27, no. 1, pp. 388–399, Jan. 2012.

Yihua Hu (M'13) received the B.S. degree in electrical motor drives, in 2003, and the Ph.D. degree in power electronics and drives, in 2011, both from China University of Mining and Technology, Jiangsu, China.

Between 2011 and 2013, he was with the College of Electrical Engineering, Zhejiang University, as a Postdoctoral Fellow. Between November 2012 and February 2013, he was an Academic Visiting Scholar with the School of Electrical and Electronic Engineering, Newcastle University, Newcastle upon Tyne, U.K. He is currently a Research Associate with the Department of Electronic & Electrical Engineering, University of Strathclyde, Glasgow, U.K. He has published more than 50 technical papers in leading journals and conference proceedings. His research interests include PV generation system, power electronics converters & control, and electrical motor drives.

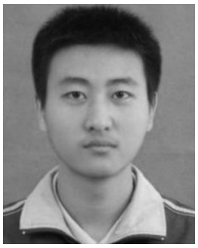

Chun Gan (S'14) received the B.S. and M.S. degrees in power electronics and drives from China University of Mining and Technology, Jiangsu, China, in 2009 and 2012, respectively. He is currently working toward Ph.D. degree in the College of Electrical Engineering, Zhejiang University, Hangzhou, China.

His research interests include electrical motor drives, motor design, control with emphasis on switched reluctance motor sensorless technique, and optimization of the torque ripple and efficiency of the motor system.

Wenping Cao (M'05–SM'11) received the B.Eng. degree in electrical engineering from Beijing Jiaotong University, Beijing, China, in 1991, and the Ph.D. degree in electrical machines and drives from the University of Nottingham, Nottingham, U.K., in 2004.

He is currently a Senior Lecturer with Queen's University Belfast, Belfast, U.K. His research interests include thermal performance and fault analysis of electric machines, drives and power electronics.

Dr. Cao received the Best Paper Award at the Linear Drives for Industry Application (LDIA'13) Conference. He serves as an Associate Editor for IEEE TRANSACTIONS ON INDUSTRY APPLICATIONS, IEEE INDUSTRY APPLICATIONS MAGAZINE, *IET Power Electronics*, and nine other International Journals. He is also a member of the Institution of Engineering and Technology and a Fellow of Higher Education Academy.

Wuhua Li (M'09) received the B.Sc. and Ph.D. degree in applied power electronics and electrical engineering from Zhejiang University, Hangzhou, China, in 2002 and 2008, respectively.

From September 2004 to March 2005, he was a Research Intern, and from January 2007 to June 2008, a Research Assistant in GE Global Research Center, Shanghai, China. From July 2008 to April 2010, he was with the College of Electrical Engineering, Zhejiang University, as a Postdoctoral Fellow, where, in May 2010, he became a Lecturer, and in December 2010, he was promoted as an Associate Professor. From July 2010 to September 2011, he was a Ryerson University Postdoctoral Fellow with the Department of Electrical and Computer Engineering, Ryerson University, Toronto, ON, Canada. His research interests include high efficiency power converters and renewable energy power conversion system. He has published more than 100 peer-reviewed technical papers and holds more than 20 issued/pending patents.

Dr. Li received the 2011 Top Ten Excellent Young Staff Award and the 2012 Distinguished Young Scholar from Zhejiang University, the 2012 Outstanding Young Researcher Award from Zhejiang Province, the 2012 Delta Young Scholar from Delta Environmental & Educational Foundation, and the 2012 National Outstanding Young Scholar. He received three Scientific and Technological Achievements Awards from Zhejiang Provincial Government and the State Educational Ministry of China in 2009 and 2011, respectively.

Stephen J. Finney received the M.Eng. degree from the Loughborough University of Technology, Loughborough, U.K., in 1988 and the Ph.D. degree from Heriot-Watt University, Edinburgh, U.K., in 1995.

For two years, he was with the Electricity Council Research Centre laboratories near Chester, U.K. He is currently a Professor with the University of Strathclyde, Glasgow, U.K. His research interests include HVDC, MMC, renewable generation, and electrical vehicle.